






Cite this: *Soft Matter*, 2018, 14, 6386

Permeability and viscoelastic fracture of a model tumor under interstitial flow†

Quang D. Tran, ‡^a Marcos *^a and David Gonzalez-Rodriguez *^b

Interstitial flow in tumors is a key mechanism leading to cancer metastasis. Tumor growth is accompanied by the development of a leaky vasculature, which increases intratumoral pressure and generates an outward interstitial flow. This flow promotes tumor cell migration away from the tumor. The nature of such interstitial flow depends on the coupling between hydrodynamic conditions and material properties of the tumor, such as porosity and deformability. Here we investigate this coupling by means of a microfluidic model of interstitial flow through a tumor, which is represented by a tumor cell aggregate. For a weak intratumoral pressure, the model tumor behaves as a viscoelastic material of low permeability, which we estimate by means of a newly developed microfluidic device. As intratumoral pressure is raised, the model tumor deforms and its permeability increases. For a high enough pressure, localized intratumoral fracture occurs, which creates preferential flow paths and causes tumor cell detachment. The energy required to fracture depends on the rate of variation of intratumoral pressure, as explained here by a theoretical model originally derived to describe polymer adhesion. Besides the well-established picture of individual tumor cells migrating away under interstitial flow, our findings suggest that intratumoral pressures observed in tumors can suffice to detach tumor fragments, which may thus be an important mechanism to release cancer cells and initiate metastasis.

Received 24th April 2018,
Accepted 13th July 2018

DOI: 10.1039/c8sm00844b

rsc.li/soft-matter-journal

1 Introduction

Interstitial flow plays an important role in the homeostasis and remodeling of living tissues.¹ In the tumor environment, interstitial flow is a key promoter of metastasis, together with biochemical changes in intercellular adhesion² and in the characteristics of the surrounding extracellular matrix.³ Interstitial flow in a tumor is driven by an abnormally high intratumoral fluid pressure due to rapid and irregular angiogenesis, the development of an abundant and leaky vasculature inside a tumor.⁴ This outwardly-directed flow promotes and guides the detachment and migration of tumor cells,^{5,6} notably by a mechanism known as autologous chemotaxis.⁷ Detached cells subsequently reach lymphatic vessels and are carried to distant tissues, initiating metastasis. Moreover, outward interstitial flow impairs drug delivery to tumors.⁸

Advancement of microfluidics has provided a useful tool to develop *in vitro* models of interstitial flow in the tumor environment. Previous microfluidics studies have modeled the tumor environment inside a microchannel by a hydrogel scaffold seeded with tumor cells. This type of setup has been used to investigate the effect of interstitial flow on cell migration in the extracellular matrix surrounding the tumor.^{9–14} Whereas many studies have focused on understanding the origin of interstitial flow and its role on the migration of cancer cells within the extracellular matrix, little attention has been given to describing the radially outgoing interstitial flow within the tumor mass, before cell detachment from the aggregate occurs.

Indeed, there is insufficient experimental data to characterize the permeability of soft tissues, due to the difficulty to determine this parameter.^{15,16} Existing *in vitro* or *ex vivo* estimates of permeability have been obtained for excised tissue samples placed in macroscopic perfusion devices, whereas *in vivo* measurements are obtained from measuring the pressure difference between two micropipette probes.¹⁵ Reported values of different soft tissue permeabilities range from 10^{-18} to 10^{-10} m², and a similar range of variability is reported for tumoral tissue.^{15–18} The complexity and internal heterogeneity of the samples used in these previous studies are insufficient to develop a biophysical understanding of how permeability at the tissue scale relates to mechanical and adhesion properties at the cellular scale.

^a School of Mechanical and Aerospace Engineering, Nanyang Technological University, Singapore. E-mail: marcos@ntu.edu.sg

^b LCP-A2MC, Institut Jean Barriol, Université de Lorraine, Metz, France. E-mail: david.gr@univ-lorraine.fr

† Electronic supplementary information (ESI) available: Supplementary methods and two movies of the experimental setup and of a typical flow experiment. See DOI: 10.1039/c8sm00844b

‡ Present address: Institut de Physique de Nice (INPHYNI), Université Côte d'Azur, Nice, France.

To investigate how tissue behaviors arise from cellular properties, an appropriate model system are multicellular spheroids, formed by aggregation or by proliferation of one or several cell types, which are widely used to study tumors *in vitro*.^{19–23} Cellular aggregates and spheroids have received much attention in recent years, and previous studies have characterized many of their key biophysical properties, including rheology,^{24–27} active contractility,²⁸ surface tension and wetting,^{29–31} elastocapillarity,³² mechanosensitivity,³³ internal dynamics,^{34,35} or detachment and fracture.³⁶ However, the important question of characterizing the permeability of a cellular aggregate remains open.

In this article, we present a new microfluidic device to investigate interstitial flow through a tumoral cellular aggregate. Our setup allows us to quantify model tumor permeability. Interestingly, we identify a bidirectional coupling between permeability and tissue mechanics: interstitial flow induces aggregate deformation and cell detachment, which in turns modifies tissue permeability and thus interstitial flow. Eventually, this coupling leads to the detachment of tumor fragments. We experimentally quantify the flow conditions leading to fracture, which are in excellent agreement with a theoretical model drawn from polymer physics, in order to test the hypothesis that intratumoral pressures observed *in vivo* can induce the detachment of tumor fragments, potentially initiating metastasis.

2 Experimental methods

2.1 Microfluidic design and fabrication

Our microfluidic design is illustrated in Fig. 1(a). The central feature is a cell chamber that contains the sample through which interstitial flow is applied. In the tumor environment, interstitial fluid leaks from blood vessels at the tumor core, flows outwardly following a negative pressure gradient, and eventually drains into lymphatic vessels outside the tumor. In our simplified geometry, fluid flows through a model tumor contained in the chamber due to a pressure gradient imposed between the inflow and outflow channels. Thus, flow through our cell chamber represents the radially outward interstitial flow through a section of the tumor, from its core to its periphery.

The cell chamber is a rectangular cuboid with a base area of $500 \times 500 \mu\text{m}^2$ and a height of $110 \mu\text{m}$. This height is a compromise between a 3D system for biological pertinence, and a quasi-2D system that allows easier quantification and better insight into the physical processes at work. The cell chamber is connected to flow input and output microchannels, as well as a sample input microchannel (see Fig. 1(a)). The sample input microchannel serves to introduce the sample into the chamber, and it is clamped afterwards. We have employed two alternative designs for the chamber, either with or without pillars. Pillars were needed to hold a hydrogel in the chamber during preliminary calibration runs (Fig. 1(b)), but they were not required to study model tumors. The design also features a narrow side channel parallel to the chamber (inset of Fig. 1(a)) to allow sufficient flow discharge, even when a sample of very

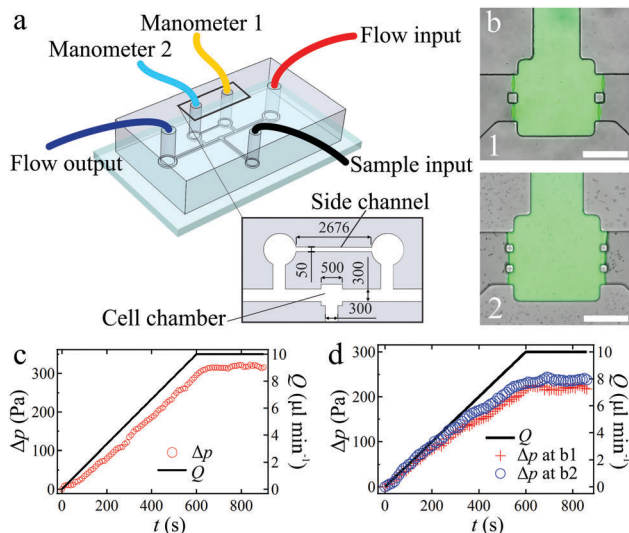


Fig. 1 Microfluidic device to characterize interstitial flow through a cellular aggregate. (a) Schematics of the microfluidic design. Lengths are in μm . (b) Two alternative cell chamber designs with multiple pillars, used for hydrogel studies. The chambers are filled with collagen gel type I at a concentration of 3 mg ml^{-1} . Scale bar: $200 \mu\text{m}$. (c) Calibration test of the side channel where flow through the cell chamber is blocked. (d) Calibration test with the cell chamber filled with collagen gel type I. The Δp versus Q relationship was measured for two different pillar configurations, corresponding to (b1) (labeled Δp at b1) and (b2) (labeled Δp at b2). The expected value of the hydrogel's intrinsic permeability $K_g \approx 1.5 \times 10^{-12} \text{ m}^2$ is retrieved.^{40,41}

low permeability is present in the cell chamber. Without this side channel, or with a less permeable side channel than the one chosen for the final design, excessive buildup of fluid pressure occurred for the less permeable samples, which created undesirable experimental artifacts and prevented measuring aggregate permeability before fracture. The total flow rate through the system was controlled by a syringe pump (KDS Legato 210P, KD Scientific, MA, USA) connected to the flow input channel. The flow output channel discharges out to the atmosphere. Each of the two ports at the entrance to and exit from the side channel was connected to a separate digital manometer (HD 755-0.5 psi, Extech Instruments, MA, USA) to measure the pressure difference across the sample.

We fabricated our microfluidic devices in PDMS (Sylgard 184, Dow Chemical, Midland, MI, USA) using standard soft-lithography technique.^{37–39} The silicon master containing the design patterns was fabricated by standard photo-lithography using SU-8 2100 (MicroChem, Newton, MA, USA) to achieve the desired thickness of $110 \mu\text{m}$. We then molded the silicon master in PDMS solution with curing agent to form PDMS chips. Holes were punched in the PDMS chip, which was then bonded onto a glass slide using plasma treatment.

2.2 Calibration of the side channel

To determine the flow rate through our device, the hydrodynamic resistance of the side channel must be measured. To this end, we fabricated a version of our microfluidic chip with a blocked cell chamber. A molded PDMS chip with punched

holes was placed on a silicon wafer. We injected a droplet of PDMS into the sample input channel, of sufficient volume to completely fill the cell chamber. We then placed the wafer with the PDMS chip inside an oven at 80 °C for 1 hour. The hardened PDMS chip was then peeled off the wafer and bonded to a glass slide using plasma treatment, which secures the adhesion of the PDMS blockage to the glass slide. A flow of culture medium at 37 °C was established through this modified version of our device. Since the cell chamber is blocked, the flow rate imposed by the pump Q goes fully through the side channel, $Q_s = Q$. By measuring the pressure difference Δp , we were able to quantify the hydrodynamic resistance of the side channel $R_s = \Delta p/Q_s$. As shown in Fig. 1(c), the imposed flow rate was increased from 0 to 10 $\mu\text{l min}^{-1}$ over the first 10 minutes, then kept constant at 10 $\mu\text{l min}^{-1}$ for another 5 minutes. We obtained $R_s = 32.18 \pm 0.13 \text{ Pa min } \mu\text{l}^{-1}$ (standard deviation, $N = 5$; see Fig. 1(c)). This corresponds to an intrinsic permeability of $K_s = \mu L_s/(R_s A_s) = 1.97 \times 10^{-10} \text{ } \mu\text{m}^2$, where $L_s = 2676 \text{ } \mu\text{m}$ is the length of the side channel, $A_s = 50 \times 110 \text{ } \mu\text{m}^2$ is the cross-sectional area of the side channel, and $\mu = 0.78 \times 10^{-3} \text{ Pa s}$ is the DMEM culture medium viscosity at 37 °C. Our calibration test also shows a rapid response of the measured pressure following changes in the imposed flow rate, which enables us to disregard unsteady effects due to changes in the flow rate. In order to assure that side channel dimensions are constant across all experiments, we produced all duplicate devices from one single mold pattern, corresponding to the calibrated device described above.

2.3 Validation of permeability measurements

To validate the permeability measurements produced by our device, we started by verifying its ability to retrieve the known intrinsic permeability of a hydrogel (Fig. 1(d)). We assume the sample in the chamber to behave as a porous medium, characterized by Darcy's law, $Q_a = \Delta p/R_a$, where Q_a is the flow rate through the sample, Δp is the pressure difference between the two manometers, and $R_a = \mu L/(K_a A)$ is the sample's hydrodynamic resistance, with μ the fluid viscosity ($\mu = 0.78 \times 10^{-3} \text{ Pa s}$ for DMEM culture medium at 37 °C⁴²), L the sample's length along the flow direction, K_a the sample's intrinsic permeability, and A the cross-sectional area. This macroscopic formulation of Darcy's law represents an average flow through the sample, without accounting for any flow heterogeneities.

In the hydrogel experiment, we coated the microchannels with poly-D-lysine (PDL) solution at 1 mg ml^{-1} (P6407, Sigma-Aldrich, St. Louis, MO, USA). We then aspirated the PDL solution and washed the devices 3 times with distilled water. The devices were dried in an oven at 40 °C for 3 hours. We prepared bovine type I collagen gel solution (A10644-01, ThermoFisher, Waltham, MA, USA) at a concentration of 3 mg ml^{-1} , then added 1% of FITC fluorescein (F1906, ThermoFisher) to render the gel fluorescent. The gel solution was micropipetted into the sample input channel and held inside the cell chamber by the pillars. The device containing the gel solution was placed for 30 minutes inside a CO₂ incubator at 37 °C, leading to gelification (Fig. 1(b)).

We then imposed a flow of culture medium at 37 °C. During flow application, the sample input channel was kept clamped.

The flow rate was progressively increased from 0 to 10 $\mu\text{l min}^{-1}$ over 10 minutes, then kept constant at 10 $\mu\text{l min}^{-1}$ for another 5 minutes. The flow rate through the gel is calculated by correcting for side channel flow: $Q_g = Q - Q_s$. The hydrodynamic resistance of the gel is $R_g = \Delta p/Q_g = R_s \Delta p/(Q R_s - \Delta p)$, with $R_s = 32.18 \text{ Pa min } \mu\text{l}^{-1}$ as obtained from the side channel calibration. The intrinsic permeability of the gel is then

$$K_g = \frac{\mu L}{R_g A},$$

where $A = 500 \times 110 \text{ } \mu\text{m}^2$ is the cross-sectional area of the gel, $\mu = 0.78 \times 10^{-3} \text{ Pa s}$ is the DMEM culture medium viscosity at 37 °C, and $L = 500 \text{ } \mu\text{m}$ is the gel's length. Fig. 1(d) shows that the measured values of Δp and Q are proportional. A linear regression through the data (not shown) yields $K_g = (1.37 \pm 0.02) \times 10^{-12} \text{ } \mu\text{m}^2$ for the gel region with 2 pillars inside and $(1.82 \pm 0.14) \times 10^{-12} \text{ m}^2$ for that with 4 pillars, which are similar to reported permeability values in previous studies.^{40,41} We thus validate our device's permeability measurements. Moreover, we conclude that the presence of up to 4 pillars has a limited effect on the permeability measurement.

2.4 Production of cellular aggregates

Cellular aggregates were produced using the technique described by Guevorkian *et al.*²⁶ from breast cancer cells of the MCF-7 cell line (HTB-22, ATCC, Manassas, VA, USA), a cell line commonly used in cellular spheroid studies.^{43–45} Cells were cultured in 89% Dulbecco's Modified Eagle Medium (DMEM), supplemented with 10% Fetal Bovine Serum (FBS) and 1% penicillin–streptomycin, and they were kept in an incubator (Heracell VIOS 160i, ThermoFisher, Waltham, MA, USA) at 37 °C and 5% CO₂. We produced spheroidal cellular aggregates from a 5 ml sample of cells suspended in CO₂-equilibrated culture medium at a concentration of $4 \times 10^5 \text{ cell ml}^{-1}$, which was placed for 20 hours inside an orbital shaker (LM-420D, Yihder Technology, Xinbei City, Taiwan) at 70 rpm and 37 °C. Different cellular aggregate sizes can be attained by tuning the initial cell seeding density, rotating speed, and cell spinning duration, as previously reported.^{46,47} Consistent with previous studies on the role of these parameters, we have observed that reducing the initial cell density resulted in a smaller number of cellular aggregates, which are also smaller in size. Increasing the rotation speed reduced the final aggregate size as well. A longer agitation time yielded larger aggregates, but cell death at the tumor core is then observed, which is attributed to lack of nutrient supply for times longer than 48 hours.

2.5 Flow experiments with cellular aggregates

To study interstitial flow through a model tumor, a cellular aggregate with a diameter larger than 400 μm was selected for each experiment. Before introducing the aggregate, the cell chamber was coated with a 100 $\mu\text{g ml}^{-1}$ solution of fibronectin (F1411, Sigma-Aldrich, St. Louis, MO, USA), an extracellular matrix protein that promotes cell adhesion. Fibronectin coating assures strong cell adhesion to the walls, thus preventing peripheral leakage and forcing the establishment of interstitial

flow through the aggregate. All microchannels were filled with CO₂-equilibrated culture medium. Then, the aggregate was micropipetted into the inlet of the sample input channel, which was then connected to the syringe pump to slowly flow the aggregate into the cell chamber (see ESI,† Movie 1). The aggregate was left inside the chamber at 37 °C for 2 hours, before applying interstitial flow. During this equilibration time, the aggregate spread on the fibronectin-coated walls, strongly adhering to them, as described by Douezan *et al.*³⁰ (Fig. 2(a)). The hydrodynamics experiment was then started by imposing the desired flow rate of CO₂-equilibrated culture medium. In some experiments, a 1% solution of FITC fluorescein (F1906, ThermoFisher) was added to the medium in order to visualize the flow paths. FITC fluorescein also allows confirming the absence of preferential leakage near the walls, thus verifying the tight adhesion of the aggregate to the channel walls.

3 Results and discussion

3.1 Permeability of a model tumor

We study the behavior of cellular aggregates when the pump is set to deliver a given flow rate Q . We emphasize that the imposed flow rate is $Q = Q_a + Q_s$, the sum of the flow rate through the aggregate, Q_a , and through the side channel, Q_s . As the imposed Q is increased, the measured pressure difference across the aggregate (Δp) increases, and the fluorescence signal shows the emergence of preferential flow paths through the aggregate, which is stretched by the applied pressure (Fig. 2(b)). Further increase of Q eventually results in a sudden drop of Δp , concomitant with the appearance of a visible crack through the aggregate (Fig. 2(c)), an event that we term “aggregate fracture” and that is associated to the detachment of aggregate

fragments (see ESI,† Movie 2). We first focus on determining aggregate permeability, before considering aggregate deformation and fracture.

Fig. 2(d) and (e) show the evolution over time of the permeability of a cell aggregate subjected to a constant flow rate, of either $Q = 20$ or $Q = 30 \mu\text{l min}^{-1}$, both of which are high enough to induce aggregate fracture. After flow is started, the system takes about one minute to equilibrate, after which an essentially constant pressure difference Δp is measured. Similar to the gel calibration study, we assume Darcy's law applicable and calculate the aggregate's hydrodynamic permeability by $K_a = \mu Q_a L / (A \Delta p)$, with L the length of the cellular aggregate, A the cross-sectional area, μ the culture medium viscosity, and $Q_a = Q - Q_s$. As shown in Fig. 2(d) and (e), the initial aggregate permeability is very small as compared to that of the side channel, and the measurement is noisy. In spite of such uncertainty, we can estimate an upper bound of the initial aggregate permeability, $K_a < 2 \times 10^{-12} \text{ m}^2$, which is within the range of tumor tissue permeabilities reported in the literature.¹⁵ The full permeability dataset is presented in the ESI,† showing a mean permeability value $K_a = (8 \pm 5) \times 10^{-13} \text{ m}^2$ (mean \pm standard error). After a time of the order of 10–20 minutes, a sudden drop of the pressure difference is observed, corresponding to aggregate fracture. After fracture, aggregate permeability significantly increases. It is noted that the permeability value measured after fracture highly varies from one fracture event to another. We emphasize that, as demonstrated by this experiment, our microfluidic device can be used to measure the permeability of other porous biological samples, provided that the sample's hydrodynamic resistance is similar to or higher than that of the side channel.

3.2 Rheology of the model tumor

The above experiments at constant Q show that interstitial flow significantly deforms and eventually fractures a cellular aggregate. We next focused on describing flow-induced aggregate deformation. We began by characterizing the rheological response of a cellular aggregate to a constant flow rate before fracture occurs. To this end, we applied a constant flow rate, ranging from $Q = 5$ to $Q = 30 \mu\text{l min}^{-1}$ for different experiments. The flow rate was kept constant for 60 minutes. Then, flow was stopped, and aggregate relaxation was monitored for another two hours. To quantify aggregate strain, we measured the length $L(t)$ spanned by the cellular aggregate along the channel, which evolved from an initial value $L(0) = L_0$ (see Fig. 2(a) and (b)). $L(t)$ was determined from images taken every 60 seconds (see ESI†). Fig. 3(a) shows the shape of $L(t)$ for one experimental run with $Q = 5 \mu\text{l min}^{-1}$. The shape of $L(t)$ exhibits a non-affine time-dependent deformation over time that is typical of a viscoelastic material subjected to a sudden stress that is later released. This behavior is well described by the Zener model, a linear combination of two springs, which model cell and tissue elasticity, and a damper, which represents tissue viscosity arising from intercellular adhesion (Fig. 3(b)). This model is similar to rheological models previously used to describe the aspiration of a cellular aggregate into a micropipette²⁶ or its

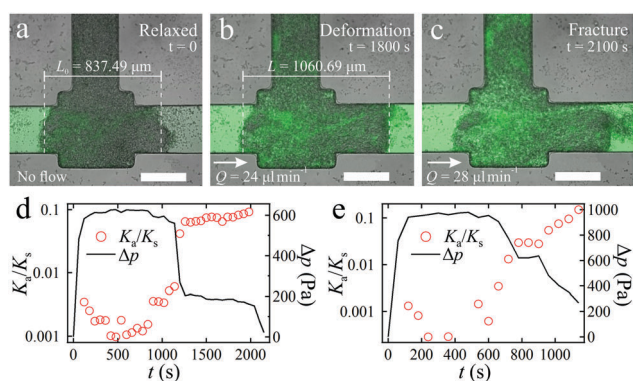


Fig. 2 Application of an interstitial flow rate through a cellular aggregate. The applied flow rate is either gradually increasing (a–c) or constant (d and e). Flow paths are visualized by a fluorescein signal. Scale bars: 300 μm . (a) The cellular aggregate was first let relax and adhere to the walls before flow was applied. (b) When exposed to a gradually increasing flow (in the direction of the arrow), the cellular aggregate deforms. (c) If Q becomes high enough ($Q = 28 \mu\text{l min}^{-1}$ for the experiment shown), fracture happens after a certain time of flow exposure. (d and e) Permeability evolution of a cellular aggregate that experiences aggregate fracture under a constant input flow rate of (d) $Q = 20$ or (e) $Q = 30 \mu\text{l min}^{-1}$. K_a/K_s represents the ratio between the intrinsic permeability of the cellular aggregate and that of the side channel ($K_s = 1.97 \times 10^{-10} \text{ m}^2$).

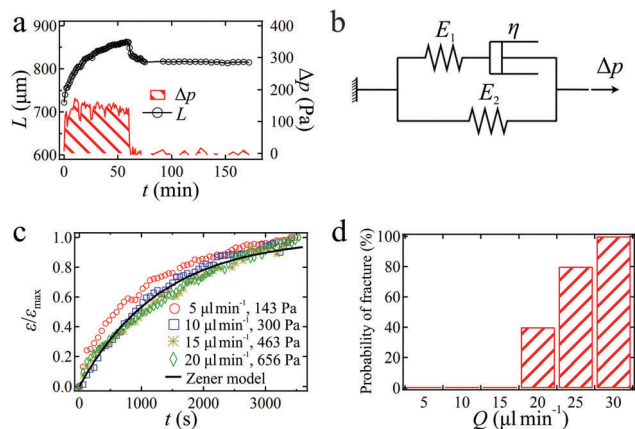


Fig. 3 Rheology of cellular aggregates under a constant Q . (a) Deformation of a cellular aggregate with $L_0 = 722 \mu\text{m}$ under $Q = 5 \mu\text{l min}^{-1}$, corresponding to $\Delta p \approx 143 \text{ Pa}$. Flow is applied for 1 h, then the flow is stopped and aggregate relaxation is observed for another 2 h. (b) The Zener model used to characterize the rheology of the cellular aggregate. The model features two springs of elastic moduli E_1 and E_2 and a damper of viscosity η . (c) Comparison between experimentally observed aggregate rheology (symbols) and fit of the Zener model (black curve). Different symbols correspond to different values of Q and Δp , as indicated in the legend. (d) Probability of aggregate fracture happening over 1 hour of application of a constant flow rate Q ($N = 5$ realizations for each Q). Probability of fracture is calculated as the ratio between the number of experimental realizations where fracture is observed divided by the total number of realizations.

stretching between two parallel plates.³⁶ Two significant differences with those previous studies are, first, that the aggregate behaves here as a viscoelastic solid rather than a viscoelastic fluid, which motivates the choice of the Zener model; second, that a residual deformation is here observed after unloading. These two features are most likely due to the different nature of cell-wall interactions: whereas in previous works the micropipette walls had been rendered non-adhesive²⁶ or there simply were no side walls,³⁶ here the channel walls are treated with fibronectin, which renders them highly adhesive. Flow-induced forces are thus insufficient to reverse cell adhesion to the wall, which prevents both long-time aggregate flow and full shape recovery after unloading. By fitting the experimental $L(t)$ curve,

we determine the Zener model parameters. The fitting procedure is explained in the ESI.† In brief, the applied pressure difference Δp is related to aggregate strain $\varepsilon = (L - L_0)/L_0$ by $\Delta p = E_2\varepsilon + \eta \frac{E_1 + E_2}{E_1} \dot{\varepsilon}$, where $\dot{\varepsilon}$ is the strain rate. The fit (Fig. 3(c)), performed for experiments where aggregate fracture did not occur, yields $E_1 = 4300 \pm 700 \text{ Pa}$, $E_2 = 1700 \pm 300 \text{ Pa}$, and $\eta = 1.6 \pm 0.4 \times 10^6 \text{ Pa s}$, which are of similar magnitude as previously reported values for cellular aggregates.^{26,36}

3.3 Fracture under interstitial flow

Once the rheology of the model tumor was described, we characterized the occurrence of aggregate fracture. The previous constant flow rate experiments showed no fracture occurrence for $Q \leq 15 \mu\text{l min}^{-1}$ ($\Delta p < 500 \text{ Pa}$), whereas the fracture probability increased for a higher flow rate (Fig. 3(d)). A previous study of fracture in cellular aggregates³⁶ showed that the threshold fracture stress of an aggregate depends on the rate at which the applied stress increases, a behavior similar to that observed in polymer detachment.⁴⁸ To investigate how fracture depends on the rate of variation of the stresses due to interstitial flow, we imposed a flow rate $Q(t)$ that linearly increases over time. Fig. 4(a) shows an example case of the evolution of $\Delta p(t)$ for a loading rate $\dot{Q} = 0.5 \mu\text{l min}^{-2}$. Δp first increases linearly with Q , reaching a maximum value, and then suddenly drops as the aggregate fractures. We term the maximum value of Δp right before fracture the critical pressure for the applied loading rate, Δp_c . Fig. 4(b) shows the dependence of Δp_c on \dot{Q} . Each loading rate was repeated for at least 5 different aggregates. We observe that Δp_c does not vary monotonically with \dot{Q} , but rather it reaches a maximum for $\dot{Q} \approx 1 \mu\text{l min}^{-2}$, indicating a maximum resistance to fracture under such loading conditions. A similar behavior was described for the detachment of polymeric glues,⁴⁸ or polymer tack, where the fracture energy $G \equiv \int \Delta p dL(t)$ depends on the deformation rate. Based on this model, we write the aggregate fracture energy as

$$G = G_0 \left\{ 1 + (\lambda - 1) \left[\arctan\left(\frac{\lambda V \tau}{l}\right) - \arctan\left(\frac{\lambda V \tau}{L_0}\right) \right] \right\}, \quad (1)$$

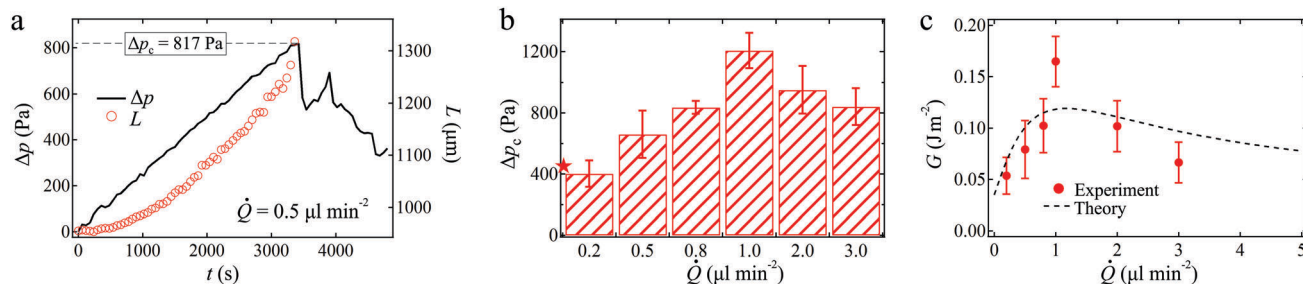


Fig. 4 Fracture of cellular aggregates under a time-varying flow. (a) Cellular aggregate deformed viscoelastically when being applied $\dot{Q} = 0.5 \mu\text{l min}^{-2}$ until fracture happened. The aggregate length L (red circles) is measured up to fracture. (b) Experimental dependence of Δp_c on \dot{Q} . Error bars are standard deviations, $N \geq 5$ aggregates for each case. The star (\star) indicates the value of Δp_c deduced for constant flow rate experiments in Fig. 3(d), which are representative of the limit case $\dot{Q} \rightarrow 0$. (c) Experimentally measured fracture energy G as a function of \dot{Q} (symbols) and theoretical model's prediction (dashed curve). Error bars are standard deviations, $N \geq 5$.

where V is the deformation speed, G_0 is the fracture energy in the limit of $V \rightarrow 0$, $\lambda = 1 + E_1/E_2 \approx 4$, $\tau = \eta/E_1 \approx 380$ s, $l \approx 110$ μm is the size of the region of stress concentration during fracture, which we scale by the smallest dimension of the microchannel, and $L_0 \approx 500$ μm is the aggregate size. Since in our experiments the time to reach fracture is significantly larger than the viscoelastic time, we estimate the speed of aggregate deformation before fracture by $V = \dot{\epsilon}L_0 \approx R_s \dot{Q}L_0/E_2$. Fig. 4(c) shows a comparison between the experimentally measured fracture energy G as a function of \dot{Q} and the model's prediction, using a fitted value of $G_0 = 0.035$ J m^{-2} , consistent with previously reported values.³⁶ According to this theoretical interpretation, the maximum energy to fracture corresponds to imposed pressure variations over the time scale of global viscoelastic tissue deformation, $(L_0\lambda\tau)/\sqrt{lL_0} \approx 50$ minutes, at which far-field viscous deformation of the aggregate contributes to resist fracture. This scaling model also describes fracture in the constant flow experiments. Because flow is imposed suddenly in these experiments, we should consider the limit $V \rightarrow \infty$, where $G \rightarrow G_0$. We can thus write the fracture condition under constant flow as $G = \Delta p(L_{\text{max}} - L_0) = (\Delta p)^2 L_0/E_2 \approx G_0$, which predicts fracture for $\Delta p > \Delta p_c \approx 350$ Pa, a reasonable estimate of the experimental value, $\Delta p_c \approx 500$ Pa. The good agreement between model and experiments suggests that the viscoelastic rheology of a model tumor can explain the effect of intratumoral pressure on fracture, an effect similar to that observed in polymer tack.

3.4 Aggregate failure at low cell–substrate adhesion

In the above experiments, the device was coated with fibronectin to secure a strong bonding between cells and channel walls. This makes cell–wall adhesion stronger than cell–cell adhesion, and aggregate fracture occurs by the formation of flow paths through the aggregate core, as discussed above. We have also performed control experiments without fibronectin coating, which are presented in the ESI.† In the absence of fibronectin, the critical pressure to fracture (Δp_c) is much lower than above. Importantly, without fibronectin, failure occurs by aggregate detachment from the channel walls, rather than by fracture at the aggregate core. Thus, in the absence of a fibronectin coating, system failure arises from limited cell–wall adhesion, in contrast to aggregate fracture due to limited cell–cell adhesion, which is observed when a fibronectin coating is applied.

4 Conclusion

In this study, we have described the viscoelastic deformation, permeabilization, and eventual fracture of a model tumor under interstitial flow. At low intratumoral pressure, the cellular aggregates studied here exhibit an intrinsic permeability of the order of 10^{-12} m^2 . As the fluid pressure increases, the model tumor deforms and its permeability increases. According to our findings, an intratumoral pressure beyond 500 Pa (~ 4 mm Hg) may yield fracture. This fracture threshold will of course depend on the cell line and on the presence and nature of an

extracellular matrix. Nevertheless, as intratumoral pressures as high as 60 mm Hg have been recorded in tumors,⁴⁹ we postulate that intratumoral pressure may induce collective cell detachment from a tumor, thus initiating cancer metastasis. Interestingly, it has been reported that pressures of comparable magnitude to those inducing fracture, of the order of the kPa, also induce protrusion formation and increased cell motility in multicellular spheroids.⁵⁰ Both mechanisms, fracture and increased cell motility, will concomitantly promote tumor dissemination. The decrease of intratumoral pressure by anti-angiogenic drug therapy⁵¹ may thus have the beneficial side effect of decreasing the risk of cell detachment. Moreover, we have shown that the fracture energy reaches a maximum for an intermediate rate of variation of intratumoral pressure, analogous to the failure of polymer glues. This maximum resistance to fracture corresponds to pressure variations over the time scale of global viscoelastic rearrangement of the tissue, of the order of one hour.³⁶ The model tumor fractures more easily for more rapid changes in intratumoral pressure, over time scales ranging from seconds to minutes, which are too fast for viscoelastic rearrangements to take place. Altogether, our work describes a biophysical mechanism by which hypertension and hypertensive spikes, where blood pressure increases by over 10 mm Hg over a few minutes, may be risk factors for cancer metastasis, as it has been reported for brain cancer patients.⁵²

Conflicts of interest

There are no conflicts of interest to declare.

Acknowledgements

We acknowledge financial support from NTU SUG Grant (M4080741.050). We thank S. H. Ling and W. Y. Chan for fruitful discussions, as well as G. Amselem, F. Brochard-Wyart, K. Guevorkian, J. Husson, and three anonymous reviewers for their careful reading and valuable insights to improve the manuscript.

References

- 1 M. A. Swartz and E. Fleury, *Annu. Rev. Biomed. Eng.*, 2007, **9**, 229–256.
- 2 W. Birchmeier and J. Behrens, *Biochim. Biophys. Acta, Rev. Cancer*, 1994, **1198**, 11–26.
- 3 D. M. Gilkes, G. L. Semenza and D. Wirtz, *Nat. Rev. Cancer*, 2014, **14**, 430–439.
- 4 Y. Boucher, M. Leunig and R. K. Jain, *Cancer Res.*, 1996, **56**, 4264–4266.
- 5 A. C. Shieh and M. A. Swartz, *Phys. Biol.*, 2011, **8**, 015012.
- 6 M. A. Swartz and A. W. Lund, *Nat. Rev. Cancer*, 2012, **12**, 210–219.
- 7 J. D. Shields, M. E. Fleury, C. Yong, A. A. Tomei, G. J. Randolph and M. A. Swartz, *Cancer Cell*, 2007, **11**, 526–538.

- 8 R. K. Jain and L. T. Baxter, *Cancer Res.*, 1988, **48**, 7022–7032.
- 9 V. Vickerman, J. Blundo, S. Chung and R. Kamm, *Lab Chip*, 2008, **8**, 1468–1477.
- 10 W. J. Polacheck, J. L. Charest and R. D. Kamm, *Proc. Natl. Acad. Sci. U. S. A.*, 2011, **108**, 11115–11120.
- 11 U. Haessler, J. C. Teo, D. Foretay, P. Renaud and M. A. Swartz, *Integr. Biol.*, 2012, **4**, 401–409.
- 12 J. Kalchman, S. Fujioka, S. Chung, Y. Kikkawa, T. Mitaka, R. D. Kamm, K. Tanishita and R. Sudo, *Microfluid. Nanofluid.*, 2013, **14**, 969–981.
- 13 W. J. Polacheck, A. E. German, A. Mammoto, D. E. Ingber and R. D. Kamm, *Proc. Natl. Acad. Sci. U. S. A.*, 2014, **111**, 2447–2452.
- 14 Y. L. Huang, C.-K. Tung, A. Zheng, B. J. Kim and M. Wu, *Integr. Biol.*, 2015, **7**, 1402–1411.
- 15 P. A. Netti and R. K. Jain, Interstitial transport in solid tumors, in *Cancer modelling and simulation*, ed. L. Preziosi, Chapman & Hall/CRC, Boca Raton, 2003, ch. 3, pp. 51–74.
- 16 A. Fahlgren, L. Johansson, U. Edlund and P. Aspenberg, *Acta Bioeng. Biomech.*, 2012, **14**, 47–51.
- 17 E. A. Swabb, J. Wei and P. M. Gullino, *Cancer Res.*, 1974, **34**, 2814–2822.
- 18 S. McGuire, D. Zaharoff and F. Yuan, *Ann. Biomed. Eng.*, 2006, **34**, 1173–1181.
- 19 W. Mueller-Klieser, *J. Cancer Res. Clin. Oncol.*, 1987, **113**, 101–122.
- 20 R.-Z. Lin and H.-Y. Chang, *J. Biotechnol.*, 2008, **3**, 1172–1184.
- 21 F. Hirschhaeuser, H. Menne, C. Dittfeld, J. West, W. Mueller-Klieser and L. A. Kunz-Schughart, *J. Biotechnol.*, 2010, **148**, 3–15.
- 22 G. Mehta, A. Y. Hsiao, M. Ingram, G. D. Luker and S. Takayama, *J. Controlled Release*, 2012, **164**, 192–204.
- 23 D. Gonzalez-Rodriguez, K. Guevorkian, S. Douezan and F. Brochard-Wyart, *Science*, 2012, **338**, 910–917.
- 24 G. Forgacs, R. A. Foty, Y. Shafrir and M. S. Steinberg, *Biophys. J.*, 1998, **74**, 2227–2234.
- 25 A. Mgharbel, H. Delanoë-Ayari and J.-P. Rieu, *HFSP J.*, 2009, **3**, 213–221.
- 26 K. Guevorkian, M.-J. Colbert, M. Durth, S. Dufour and F. Brochard-Wyart, *Phys. Rev. Lett.*, 2010, **104**, 218101.
- 27 A. Blumlein, N. Williams and J. J. McManus, *Sci. Rep.*, 2017, **7**, 7346.
- 28 K. Guevorkian, D. Gonzalez-Rodriguez, C. Carlier, S. Dufour and F. Brochard-Wyart, *Proc. Natl. Acad. Sci. U. S. A.*, 2011, **108**, 13387–13392.
- 29 M. S. Steinberg, *Science*, 1963, **141**, 401–408.
- 30 S. Douezan, K. Guevorkian, R. Naouar, S. Dufour, D. Cuvelier and F. Brochard-Wyart, *Proc. Natl. Acad. Sci. U. S. A.*, 2011, **108**, 7315–7320.
- 31 S. Douezan, J. Dumond and F. Brochard-Wyart, *Soft Matter*, 2012, **8**, 4578–4583.
- 32 F. Mazuel, M. Reffay, V. Du, J.-C. Bacri, J.-P. Rieu and C. Wilhelm, *Phys. Rev. Lett.*, 2015, **114**, 098105.
- 33 F. Montel, M. Delarue, J. Elgeti, L. Malaquin, M. Basan, T. Risler, B. Cabane, D. Vignjevic, J. Prost, G. Cappello and J.-F. Joanny, *Phys. Rev. Lett.*, 2011, **107**, 188102.
- 34 M. Delarue, F. Montel, O. Caen, J. Elgeti, J.-M. Siaugue, D. Vignjevic, J. Prost, J.-F. Joanny and G. Cappello, *Phys. Rev. Lett.*, 2013, **110**, 138103.
- 35 G. Beaune, T. Vasilica Stirbat, N. Khalifat, O. Cochet-Escartin, S. Garcia, V. V. Gurchenkov, M. P. Murrell, S. Dufour, D. Cuvelier and F. Brochard-Wyart, *Proc. Natl. Acad. Sci. U. S. A.*, 2014, **111**, 8055–8060.
- 36 D. Gonzalez-Rodriguez, L. Bonnemay, J. Elgeti, S. Dufour, D. Cuvelier and F. Brochard-Wyart, *Soft Matter*, 2013, **9**, 2282–2290.
- 37 G. M. Whitesides, E. Ostuni, S. Takayama, X. Jiang and D. E. Ingber, *Annu. Rev. Biomed. Eng.*, 2001, **3**, 335–373.
- 38 Q. D. Tran, T. F. Kong, D. Hu, Marcos and R. H. Lam, *Lab Chip*, 2016, **16**, 2813–2819.
- 39 T. F. Kong, X. Shen, Marcos and C. Yang, *Appl. Phys. Lett.*, 2017, **110**, 233501.
- 40 V. Serpooshan, T. M. Quinn, N. Nuja and S. N. Nazhat, *Acta Biomater.*, 2013, **9**, 4673–4680.
- 41 O. Moreno-Arotzena, J. G. Meier, C. del Amo and J. M. Garcia-Aznar, *Materials*, 2015, **8**, 1636–1651.
- 42 C. Wang, H. Lu and M. A. Schwartz, *J. Biomech.*, 2012, **45**, 1212–1218.
- 43 A. Fritsch, M. Höckel, T. Kiessling, K. D. Nnetu, F. Wetzel, M. Zink and J. A. Käs, *Nat. Phys.*, 2010, **6**, 730–732.
- 44 P. Sabhachandani, V. Motwani, N. Cohen, S. Sarkar, V. Torchilin and T. Konry, *Lab Chip*, 2016, **16**, 497–505.
- 45 S. Raghavan, P. Mehta, E. N. Horst, M. R. Ward, K. R. Rowley and G. Mehta, *Oncotarget*, 2016, **7**, 16948–16961.
- 46 J. M. Kelm, N. E. Timmins, C. J. Brown, M. Fussenegger and L. K. Nielsen, *Biotechnol. Bioeng.*, 2003, **83**, 173–180.
- 47 S. L. Nyberg, J. Hardin, B. Amiot, U. A. Argikar, R. P. Rimmel and P. Rinaldo, *Liver Transplant.*, 2005, **11**, 901–910.
- 48 F. Saulnier, T. Ondarçuhu, A. Aradian and E. Raphaël, *Macromolecules*, 2004, **37**, 1067–1075.
- 49 C.-H. Heldin, K. Rubin, K. Pietras and A. Östman, *Nat. Rev. Cancer*, 2004, **4**, 806–813.
- 50 K. Alessandrini, V. V. Sarangi, V. V. Gurchenkov, B. S. Inha, T. B. Kiessling, L. Fetler, F. Rico, S. Scheuring, C. Lamaze, A. Simon, S. Geraldo, D. Vignjevic, H. Doméjean, L. Rolland, A. Funfak, J. Bibette, N. Bremond and P. Nassoy, *Proc. Natl. Acad. Sci. U. S. A.*, 2013, **110**, 14843–14848.
- 51 J. M. Munson and A. C. Shieh, *Cancer Manage. Res.*, 2014, **19**, 317–328.
- 52 A. E. Sahnoun, L. D. Case, S. Chavour, S. Kareem and G. G. Schwartz, *Anticancer Res.*, 2004, **24**, 3115–3120.